The effect of fault architecture on slip behavior in shale revealed by distributed fiber optic strain sensing

Chet Hopp[1,1], Yves Guglielmi[1,1], Antonio Pio Rinaldi[2,2], Florian Soom[1,1], Quinn Wenning[3,3], Paul Cook[1,1], Michelle Robertson[1,1], Maria KAKURINA[4,4], and Alba Zappone[3,3]

[1]Lawrence Berkeley National Lab
[2]ETH Zurich,Lawrence Berkeley National Laboratory
[3]ETH Zurich
[4]University of Neuchâtel

November 30, 2022

Abstract

We use Distributed Strain Sensing (DSS) through Brillouin scattering measurements to characterize the reactivation of a fault zone in shale (Opalinus clay), caused by the excavation of a gallery at 400 m depth in the Mont Terri Underground Laboratory (Switzerland). DSS fibers are cemented behind casing in six boreholes cross-cutting the fault zone. We compare the DSS data with co-located measurements of displacement from a chain potentiometer and a three-dimensional displacement sensor (SIMFIP). DSS proves to be able to detect in- and off-fault strain variations induced by the gallery excavated 30-50 m away. The total permanent displacement of the fault is 200 microns at rates up to 1.5 nm/sec. DSS is sensitive to longitudinal and shear strain with measurements showing that fault shear is concentrated at the top and bottom interfaces of the fault zone with little deformation within the fault zone itself. Such a localized pattern of strain relates to the architecture of the fault that is characterized by a thick, weak layer, slipping at the edges, with no surrounding damage zone. Overall, DSS shows that slow slip may activate everywhere there is a weak fault within a shale series. Thus, our work demonstrates the importance of shear strain on faults caused by remote loading, highlighting the utility of DSS systems to detect and quantify these effects at large reservoir scales.

The effect of fault architecture on slip behavior in shale revealed by distributed fiber optic strain sensing

Chet Hopp[1], Yves Guglielmi[1], Antonio Pio Rinaldi[2,1], Florian Soom[1], Quinn Wenning[4], Paul Cook[1], Michelle Robertson[1], Maria Kakurina[5], and Alba Zappone[2,3]

[1]Lawrence Berkeley National Laboratory; Earth and Environmental Sciences Area, Berkeley, CA, USA
[2]Swiss Seismological Service, ETH Zürich, Zürich, Switzerland
[3]Department of Mechanical Engineering, ETH Zürich, Zürich, Switzerland
[4]Department of Earth Sciences, ETH Zürich, Zürich, Switzerland
[5]University of Neuchâtel, CHYN, Emile-Argand 11, 2000, Neuchâtel, Switzerland

Key Points:

- Slow slip on a fault zone in a clay caprock concentrates on two interfaces with the intact host rock, because the fault displays no damage zone.
- Distributed strain sensing (DSS) shows equal measurand performance to standard borehole potentiometers, with better spatial resolution and sensitivity to shear.
- Activated and unactivated fractures share similar orientations; activated fractures are weaker due to the presence of scaly clay.

Corresponding author: Chet Hopp, `chopp@lbl.gov`

Abstract

We use Distributed Strain Sensing (DSS) through Brillouin scattering measurements to characterize the reactivation of a fault zone in shale (Opalinus clay), caused by the excavation of a gallery at ∼400 m depth in the Mont Terri Underground Laboratory (Switzerland). DSS fibers are cemented behind casing in six boreholes cross-cutting the fault zone. We compare the DSS data with co-located measurements of displacement from a chain potentiometer and a three-dimensional displacement sensor (SIMFIP). DSS proves to be able to detect in- and off-fault strain variations induced by the gallery excavated 30–50 m away. The total permanent displacement of the fault is ∼200 microns at rates up to 1.5 nm/sec. DSS is sensitive to longitudinal and shear strain with measurements showing that fault shear is concentrated at the top and bottom interfaces of the fault zone with little deformation within the fault zone itself. Such a localized pattern of strain relates to the architecture of the fault that is characterized by a thick, weak layer, slipping at the edges, with no surrounding damage zone. Overall, DSS shows that slow slip may activate everywhere there is a weak fault within a shale series. Thus, our work demonstrates the importance of shear strain on faults caused by remote loading, highlighting the utility of DSS systems to detect and quantify these effects at large reservoir scales.

1 Plain language summary

Understanding how and why faults move in anisotropic shales is important for assessing the integrity of caprocks overlying geologic CO_2 sequestration sites or increasing efficiency of hydraulic fracturing operations in shale gas reservoirs. Here we show that fiber optic cables can be used to accurately measure fault slip when cemented inside boreholes that intersect such a structure. This allows detecting and monitoring of a larger volume of rock than ever before. Our measurements show that a kilometers-long fault in a clay rock, when disturbed by the excavation of a tunnel ∼30 m away, displayed localized slip mostly along its upper and lower interfaces, in contrast to a more distributed slip as would be expected with a more "classical" fault core-damage zone architecture. In addition, the excavation produced slip on other, smaller fractures, with slip on these planes sometimes exceeding the slip on the larger fault. These observations show how important slow slip in anisotropic shales can be in accommodating remote loading (e.g. deep reservoir pressurization or hydraulic fracturing). DSS offers new insight into whether slow slipping faults can trigger significant caprock leakage and induce earthquakes during deep injection operations.

2 Introduction

Understanding the mechanics of fault and fracture movement in anisotropic shales is important for estimating the integrity of caprocks overlying geologic CO_2 sequestration sites or for improving the efficiency of hydraulic fracturing stimulations of shale gas reservoirs. Indeed, by combining reservoir-scale, geophysical data with laboratory results, Zoback et al. (2012) suggest that hydrofracturing might cause significant slow slip on surrounding fractures and faults in shale rocks, particularly when clay content exceeding 30% favors stable sliding instead of unstable slip (i.e. microseismicity). Looking at the decameter scale around underground galleries in the Opalinus clay shales in Mont Terri Rock Laboratory (Switzerland), Amann et al. (2018) highlight that a high density of bedding planes and faults strongly influences macroscopic failure through shearing along pre-existing planes coupled to newly created extensional fractures. Compiling laboratory determined mechanical properties of various types of shales, Bourg (2015) shows a factor of 20 decrease of the unconfined compressive strength of shales that contain $\sim$1/3 phyllosilicate (clay mineral) mass fraction. It is therefore important to better characterize how rupture can develop macroscopically in a thick shale layer since it may substantially change stress and favor leakage flowpath creation. For example, field experiments (Guglielmi et al., 2020) and laboratory tests (Gutierrez et al., 2000) show that even small amounts of shear can lead to significant modifications of the hydraulic properties of fractured and mechanically anisotropic shales.

Given this context, optical fiber-based sensors may offer the possibility to track how widely-distributed shear may be in thick anisotropic shale series. A broad array of scientific and engineering applications have sprung up in the past few decades around the use of fiber optics as distributed measurement devices (so-called distributed fiber optic sensing, DFOS). These techniques leverage light that is scattered in the opposite direction of a passing optical pulse and, by measuring the frequency and gain of these backscattered components, can be used for sensing purposes. The result is a quasi-continuous sensor capable of being deployed in harsh environments and over distances of several kilometers (Hartog, 2017).

In this study we focus on measurements of the longitudinal strain of the sensing fiber through interrogation of the Brillouin component of backscattered light. Distributed Brillouin sensing (referred to here as distributed strain sensing, DSS) has found myriad applications since its inception in the 1990's, mostly monitoring the state-of-health of various elements of critical infrastructure including the telecommunications fibers themselves (Tateda et al., 1990), the underground tunnels that house them (Naruse et al., 2005), nuclear waste repositories (Delepine-Lesoille et al., 2012), roads (Iten et al., 2008), levees (Naruse, 1999), and the stability of critical slopes (jun Wang et al., 2008).

Distributed fiber optics have also been deployed in deep boreholes, initially for monitoring of borehole casing integrity in oil and gas reservoirs (Zhou et al., 2010) but, more recently, downhole DSS has been used to monitor pumping-induced compaction (C.-C. Zhang et al., 2018), track the progression of hydraulic fractures in unconventional oil and gas reservoirs (Z. Zhang et al., 2020), and measure injection-induced strains in shallow aquifers (Sun et al., 2020). While these studies convincingly demonstrated the ability of DSS to measure strains on the order of tens of microstrains ($\mu\epsilon$), borehole-based measurements are inherently difficult to verify due to inaccessibility and the difficulty of deploying separate instruments within a single borehole.

Two previous studies have made an attempt to ground truth DSS strain measurements in grouted boreholes. Krietsch et al. (2018) monitored a series of hydraulic stimulation tests in the Grimsel underground lab with co-located DSS and Fiber Bragg Gratings (FBGs). Using the FBG system as the 'true' measure, the authors determined that the DSS system provided good qualitative agreement with the FBG system but poor temporal and measurand resolution. They also observed poor agreement in the magnitude of the measured strains. Valley et al. (2012) grouted fibers into a sill pillar that was actively undergoing mining and attempted to corroborate the measurements using co-located extensometers. They also concluded that, while the DSS measurements were qualitatively in agreement with the extensometer, the measurements were not useful in quantifying the strain in the borehole. Both of these studies highlight the ongoing need for field testing and independent corroboration of DSS measurements in grouted boreholes.

Here we present measurements from a suite of seven boreholes intersecting a fault, hereafter referred to as the Main Fault, in the Mont Terri Rock Laboratory (MTRL, Switzerland). These boreholes are part of an experimental setup aimed at studying the effect of CO_2 injection and pressurization (CS-D and FS-B projects; Zappone et al., 2020; Guglielmi et al., 2018) on the deformation and permeability of a fault zone affecting the Opalinus clay, a low permeability rock considered an analog to a reservoir caprock (Bossart et al., 2017). Six of the seven boreholes are instrumented with a loop of single-mode fiber optic cable, grouted behind casing or anchored to inflatable packer assemblies. The boreholes also contain displacement sensors, including a chain potentiometer and a three-dimensional displacement sensor called the SIMFIP (Guglielmi et al., 2013), which are co-located/proximal with the fiber optic loops and allow us to tune our DSS measurements.

Our study details the mechanical response of the thick, faulted, and anisotropic Opalinus clay to stress transfered from the excavation of a new gallery in the MTRL. We first use this opportunity to demonstrate the sensitivity of our multi-borehole fiber array to the movement occurring within the Main Fault zone in response to a remote triggering event. We then use these measurements to characterize the macroscopic activation of the various Opalinus clay structures. Thanks to the independent displacement measurements from co-located or proximal sensors with respect to the fibers, we demonstrate clear consistency between the strain magnitude and temporal occurrence captured between sensors. We discuss how stress and fault weakness related to its material content and architecture control the observed distributed slip.

2.1 Fault activation experiments at the Mont Terri Rock Laboratory

The Mont Terri Rock Laboratory, operated by the Swiss Geological Survey, is located on one limb of a fault-bend anticline within a low-permeability claystone unit known as the Opalinus clay (Bossart et al., 2017; Hostettler et al., 2017). The Opalinus clay is both a potential target formation for Switzerland's nuclear waste repositories and a useful cap rock analog for CO_2 sequestration (Bossart et al., 2017). Additionally, the galleries of the MTRL are intersected by a kilometer-scale thrust fault zone, the so-called Main Fault (Jaeggi et al., 2017), which offers researchers the opportunity to investigate the effect of fault activation on the leakage potential of a self-sealing clay unit (Guglielmi et al., 2017, 2020; Birkholzer, 2018; Zappone et al., 2020). The Mont Terri Main Fault consists of a thrust zone, 1 to 3 m in width, bounded by two major fault planes characterized by a strike of N066^o to N075^o and a dip of 45^o to 65^{o}SE (Figure 1).

The CS-D and FS-B projects, directed by ETH Zürich and Lawrence Berkeley National Lab (LBNL), respectively, are focused on understanding how a minor fault affecting a clay unit (i.e. caprock) might respond to the long term injection of CO_2 (Zappone et al., 2020). The two projects are highly complementary. The CSD project is looking at small ∼0.05 ml/min injection of a CO_2 brine into the fault below the fault activation pressure. It is mainly focusing on long term hydro-mechanical and chemical processes of fluid diffusion at meter-scale in the fault zone (Zappone et al., 2020). The FS-B project is looking at large-scale (>5 L/min) injection into the fault above activation pressure. It is focused on hydromechanical processes at 10-meter scale during fault rupture, including the potential for induced seismicity, and during inter-rupture periods (Guglielmi et al., 2018).

A 70-m x 70-m x 70-m volume, crosscut by the Main Fault, is instrumented with 23 boreholes hosting various systems recording pressure and flow rate into multiple injection intervals, active and passive-source seismicity, electrical resistivity, fluid and gas geochemistry, and geomechanical strain/displacement/tilt. Figure 1 shows all boreholes drilled by CS-D/FS-B. Here we focus on the CS-D boreholes (colored in the foreground of Figure 1). The FS-B boreholes are shown in gray in the background.

3 Monitoring network and remote gallery excavation

The depth of the Main Fault zone intersection with each borehole, as verified by image logging and core, varies from 11 to 28 m below the gallery floor (Table 1). The thickness of the fault zone varies between 1 and 3 meters within the MTRL and is characterized by a laterally heterogeneous mix of fault gouge, C'-type shear bands, scaly clay, and meso- and micro-scale folds (Nussbaum et al., 2011). Here 'scaly clay' refers to a mass of unaltered, Opalinus microlithons, separated by slickensides, and is pervasive throughout the Main Fault (Jaeggi et al., 2017). Fault planes within the Main Fault zone are mostly oriented subparallel to the fault zone itself, but also include a set of fractures normal to it (Zappone et al., 2020; Wenning et al., 2020). In addition, a series of ENE-striking, bedding-parallel fractures, with similar strike but shallower dip than the Main Fault, are intersected by the CS-D boreholes (Zappone et al., 2020). Bedding in the Opalinus is oriented subparallel to the Main Fault, striking N055^o, and dipping SE046^o, roughly 15^o shallower than the Main Fault.

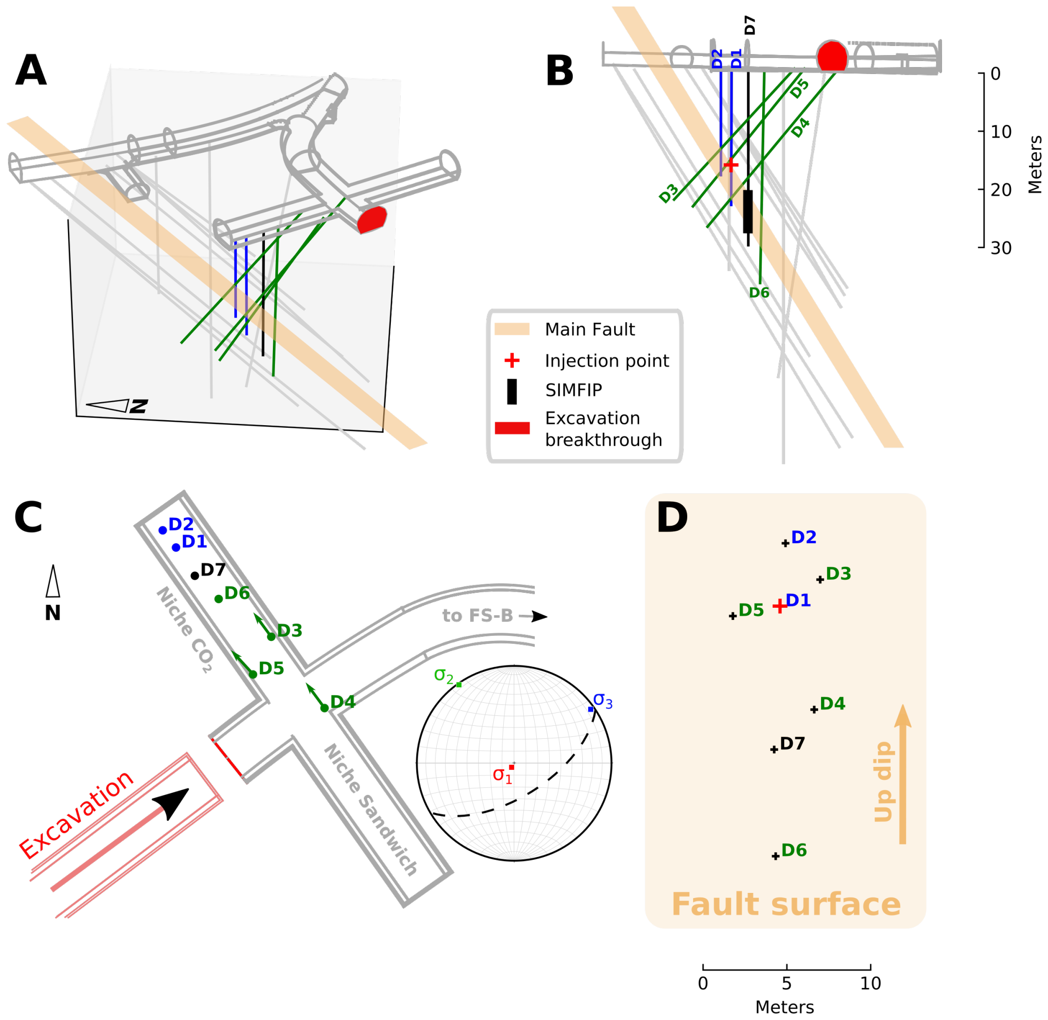

Figure 1. A) 3D perspective of the FS-B/CS-D project showing all boreholes colored by use. Blue boreholes D1 & D2 are injection and pressure monitoring boreholes, green boreholes contain monitoring systems, and the black borehole, D7, contains the SIMFIP displacement sensor. Light gray boreholes in the background are FS-B boreholes. All boreholes are instrumented with distributed fiber optic sensors except D7 B) Cross-section along Niche CO_2 with the injection point in D1 indicated by a red cross. C) Map view of the borehole collar locations in Niche CO_2 and lower hemisphere stereonet projection of the principal stress axes estimated by Guglielmi et al. (2020). Dotted line shows the approximate orientation of the Main Fault D) Intersection points for each well with the top of the Main Fault

Borehole name	Main Fault top [m]	Main Fault bottom [m]
BCS-D1	14.34	19.63
BCS-D2	11.04	16.39
BCS-D3	17.98	20.58
BCS-D4	27.05	28.44
BCS-D5	19.74	22.66
BCS-D6	28.5	31.4
BCS-D7	22.46	25.54

Table 1. Depths of the top and bottom of the Main Fault zone in each of the CS-D boreholes

Boreholes BCS-D1 through D6 contain a single 3.2 mm-diameter loop of BRUsens$^{\mathrm{TM}}$ strain sensing cable that itself comprises a single optical fiber hermetically sealed and strain-locked within a metal tube and an outer nylon sheath. These cables are designed to measure strains of up to 1% (10000 $\mu\epsilon$). In BCS-D1 and D2 (blue boreholes, Figure 1), the fiber optic cable (BRUSens 3.2 mm V4 metallic) is anchored by a compression ferrule at the top of each injection interval (with four and six intervals in D1 and D2, respectively). However, the fiber optic cables in these boreholes were not monitored at the time of the excavation detailed here and so are omitted from the data analysis.

In boreholes BCS-D3, D4, D5, and D6, the fiber (BRUSens 3.2 mm V9 grip) is cemented behind the PVC casing using a grout mix of 81.9 L water, 4.9 kg bentonite, and 50.1 kg cement (green boreholes, Figure 1). This provides a truly continuous measurement along the entire length of each borehole. In these cases, the nylon cable jacket is textured to provide optimized strain coupling between the fiber and the grout so that, in theory, only the grout strain is being measured, with the assumption made that the grout is coupled to the host rock. Each of these boreholes also includes a single resin 'plug' to mitigate against fluid traveling along the cemented annulus (Figure 2B). These plugs are 0.5–2 m thick sections where the resin replaces the grout in the annulus between the borehole wall and the PVC casing. Borehole diameter ranges from 101 to 146 mm, with consistent PVC casing diameters of 80 mm.

The fiber loops in each borehole are connected into a multi-borehole circuit and interrogated by an Omnisens DITEST VISION Dual temperature and strain unit using the Brillouin Optical Time Domain Analysis technique (Horiguchi & Tateda, 1989).

In borehole BCS-D5, a chain of 12 potentiometers is cemented behind casing alongside the fiber-optic loop in borehole BCS-D5 (Zappone et al., 2020; Rinaldi et al., 2020). Each potentiometer is connected to the adjacent units by a PVC tube and measures borehole axial displacement relative to the neighboring units with a maximum displacement of 100 mm. This chain of potentiometers provides a co-located measurement of displacement with respect to the optical fibers, allowing us to directly verify the measurements made with the DSS system.

In borehole BCS-D7, a combined three-dimensional-displacement, pressure, and fluid electrical conductivity probe, the SIMFIP (Guglielmi et al., 2013), is clamped above and below the Main Fault. The clamps are 6.3 meters apart allowing the SIMFIP to measure the relative displacement across the entire Main Fault zone. The instrument uses six fiber-bragg gratings attached to a bespoke aluminum cage to resolve the full 3D displacement field with micrometer precision. The SIMFIP is alone in BCS-D7, and therefore is not co-located with any portion of the fiber optic loop. Understanding this limitation, here we use its three-dimensional fault displacement measurement in comparison to the DSS data.

4 Excavation of Gallery 18

Excavation of Gallery 18 began on 14 March 2018, and lasted for more than one year. During much of this time, the excavation front was far from Niche CO_2, which, itself, was completed in May 2018. The installation of the CS-D systems occurred between August and December 2018. During the first half of 2019, the final stages of excavation proceeded towards Niche CO_2 as indicated in Figure 1. Excavation passed along the strike of the Main Fault at a constant $\sim$23 m distance from the upper fault zone interface. Breakthrough occurred adjacent to the CS-D experiment on 27 May 2019 (red faces in Figure 1). Prior to the breakthrough, movement was not detected by the SIMFIP and potentiometers at CS-D until 22 May 2019, when the excavation front was $\sim$26 m from the SIMFIP. Coincidentally, 22 May was also the date that the DSS system began recording. We therefore focus on the period between 22 May and 3 June 2019.

5 Methods and processing

5.1 Distributed strain sensing

When a laser pulse is sent along an optical fiber, some amount of that light is scattered backwards by its interaction with changes in the refractive index of the fiber. There are three components of this backscattered light relevant to DFOS: one is elastic (Rayleigh) and two are inelastic (Raman and Brillouin). We are concerned here with the Brillouin component, which arises from an incident photon's interaction with crystal lattice vibrations that hold some of the optical fiber's heat. As the interaction is inelastic, the backscattered light is frequency shifted by some amount that linearly depends on the temperature and strain in the fiber. This relationship is described by Horiguchi and Tateda (1989) as:

$$\Delta\nu_B = \frac{\partial\nu_B}{\partial\epsilon}\Delta\epsilon + \frac{\partial\nu_B}{\partial T}\Delta T \tag{1}$$

where $\Delta\nu_B$ is the change in Brillouin frequency shift for given changes in strain, $\Delta\epsilon$, and temperature, ΔT. $\frac{\partial\nu_B}{\partial\epsilon}$ and $\frac{\partial\nu_B}{\partial T}$ are the strain and temperature change coefficients, respectively, which for this work are 500 MHz/% and 1.0 MHz/^{o}C.

Using Equation 1, the DITEST interrogator determines the combined temperature and strain contribution to the measured Brillouin frequency shift. Each measure is then related to a given point along the fiber by recording the launch and arrival time of the probe pulse with respect to the speed of light. Because the light pulse from the interrogator has a finite length, measurements are averaged over the corresponding length of fiber. This is referred to as the spatial resolution (or often the 'gauge length'). The Brillouin frequency shift for one gauge length is reported as a single measurement at a point along the fiber that we call a 'channel'. The spatial sampling and spatial resolution were 0.26 and 0.5-to-1.0 meters, respectively, for each of the periods of our study. Notice that the channel spacing is less than the spatial resolution. Therefore, the DSS measurement is a sliding window with a width equal to the spatial resolution, slid along the fiber in increments defined by the spatial sampling.

Because the Brillouin frequency shift is sensitive to both temperature and strain changes, a number of methods are employed to deconvolve their contributions. Often, an independent measurement of temperature (for example from a Raman scattering system) is used to remove the temperature contribution from the Brillouin measurements. Alternatively, a "strain free" cable is somehow decoupled from the system of interest and can be co-located with a coupled cable and connected in series. In our case we had access to neither, but we make the assumption that the temperature change within our testbed is negligible with respect to the changes in Brillouin shifts being measured (Madjdabadi et al., 2014, 2016; Hartog, 2017).

5.2 Borehole mapping and measurement symmetry

As mentioned above, for any given distributed strain measurement, its distance along the fiber is accurately known from the two way travel time in relation to the speed of light. Translating this distance into a borehole coordinate requires a process of 'mapping' whereby the distances along-fiber are matched to the known locations of the features we want to measure (in this case boreholes BCS-D1–D6). We decide to map distance to location by observing a single Brillouin frequency shift measurement along the entire fiber length (i.e. one time sample; Figure 2A). Because the fiber is installed as a loop in each borehole, we expect there to be symmetry in the measurements about the bottom of the boreholes. In other words, the downgoing and upgoing legs of the fiber in a given borehole should measure roughly the same strain.

For the case of our experiment, the BRUsens cable is grouted into the boreholes (or attached to the casing above the packers in D1 and D2) while the sections of fiber between boreholes are standard patch cables lying in a cable tray along the gallery wall. The difference in fiber coating and installation produce an obvious difference in the Brillouin frequency measurement that allows us to map the along-fiber distances corresponding to the entry and exit points for each borehole. In Figure 2A, the entry and exit points for each borehole are indicated by dotted lines, with the bottom shown as a single solid line. The mapped along-fiber lengths agree with field measurements of the cable lengths set in the gallery. By manually selecting the point of greatest symmetry for each borehole and accounting for their known drilled depths, we isolate the slice corresponding to each borehole.

The process of borehole mapping should, in theory, result in two parallel sections (legs) of fiber in each borehole; one downgoing and one upgoing. Assuming that each is measuring approximately the same strain field, the measurements should be equal be-

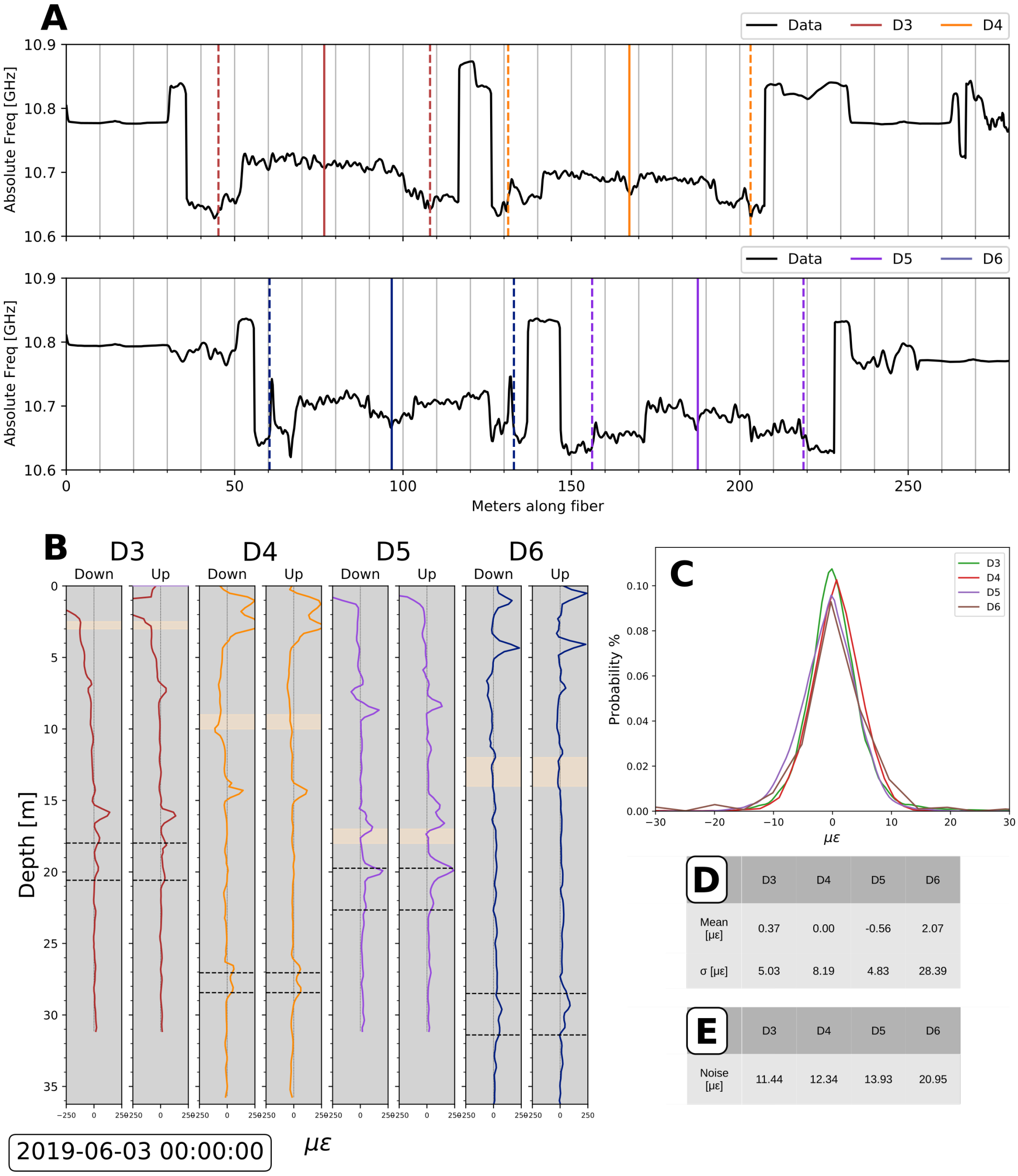

Figure 2. A) Absolute frequency along the length of the fiber during gallery excavation. The two panels correspond to two separate fiber optic loops, each with two boreholes. Boreholes D1 and D2 were not monitoring during the excavation. B) Distributed strains on the down and up-going leg of each on 3 June 2019, following the breakthrough of the excavation front on 27 May 2019. The depth to the Main Fault is marked with dotted lines, resin plugs are shown in beige. C) Kernel density estimates for the difference between the up-going and down-going legs of fiber in each borehole D) Statistics describing the difference between down and up-going fibers for each borehole E) Average 3-standard-deviation noise for each borehole.

tween up and down-going fiber for a given depth. Figure 2B shows both the down and up-going fiber leg in each borehole on 3 June 2019, following the breakthrough of the excavation on 27 May. The symmetry in the measurements between fiber legs is visually apparent. The depths at which the measurements are not symmetric typically coincide with depths where the fiber is expected to be poorly coupled to the rock mass, for example at the borehole collar or at the depths where grout is replaced by the resin plugs (beige bands, Figure 2B). But while the symmetry of the measurements between down and upgoing legs is evident, the absolute value measured at a given depth on either leg can vary significantly. This is likely a result of heterogeneous coupling of the fiber to grout and the grout to the rock mass. This could be the result of changes in the distribution of grout (e.g. air pockets) or to the effect of other equipment installed in the borehole. For example, in BCS-D5 the chain potentiometer might affect the strain measured on the fiber closest to it, but have less effect on the opposing leg. Also, for the inclined, grouted boreholes, the stress state may vary along the borehole circumference. In this case, fiber legs on opposing sides of the borehole could measure different responses to stress perturbation, even for the same depth in the borehole.

Figure 2C shows the difference between down and upgoing fiber measurements for all measurement times and channels, colored by borehole. The statistics for the distributions shown in Figure 2C are reported in Figure 2D. The fact that the distributions are nearly zero-mean signifies that there is no systematic preference for higher or lower values measured by one leg with respect to the other. The standard deviations of the curves in Figure 2D, however, range from 4.83 to 28.39 $\mu\epsilon$. This means that the measured strain at a given depth in a borehole might vary by tens of microstrains depending on which leg is selected, significantly increasing the uncertainty in the measured strain.

5.3 Measurement noise

We quantify the measurement noise following Madjdabadi et al. (2016). For each channel in a borehole, we calculate 3 standard deviations for a reference time period (with no expected strain signal). We then average this value over all channels in the sensor, resulting in a single noise value per borehole (Figure 2E). The noise levels range from 11.44 to 20.95 $\mu\epsilon$, meaning that each segment of the fiber cannot confidently resolve strains of less than these values.

5.4 Measurement artifacts

Two final artifacts are then removed from the data. The first artifact is an ambiguity in the exact position of each channel. The ambiguity arises because the channel location is reported at the center of the light pulse (for our tests 1.0-m long). But the strain could be concentrated at any point (or points) inside the pulse. We follow Madjdabadi et al. (2016) and apply a realignment step detailed in the supplements.

The second artifact is a series of systematic shifts in the measured strain for all points in the fiber. These apparently correlate with shifts in the gain of the signal returned to the interrogator, although the two values should not be related. We undertook a process of removing these shifts for times where the gain also shifted. This process is also detailed in the supplements.

6 Results

On 22 May 2019, the DSS system was turned on and began to record signals within the Main Fault zone associated with the excavation of Gallery 18. From 23 May until the breakthrough on 27 May, there were three episodes of excavation, with the excavation front advancing between 1 and 3 m during each episode. Each episode induced movement on a number of discrete features, including the Main Fault. For each excavation pulse, the activated features moved at up to 1.5 nm/sec at the onset and decelerated towards a new steady state before accelerating again in response to the next pulse.

6.1 Distribution of deformation revealed by DSS measurements

Fiber-optic strains localized on a number of discrete features within the entire shale series (Figure 3A). The deformations in the shallow zone (from 0–7 m deep) are up to one order of magnitude larger than those measured deeper than $\sim$7 m (Figure 3B). Boreholes D3 and D5 show contractions of $>$800 and $\sim$600 $\mu\epsilon$, respectively. In contrast, D4 and D6 each show two smaller-magnitude peaks of extensional strain, each $\leq$200 $\mu\epsilon$. The differences between the shallow strains in each borehole indicate a complicated strain distribution in and around the intersection of Gallery 18 and the nearby niches (Figure 1). In addition, our data show discrete spikes in the strain, highlighting that the deformation is not broadly distributed but is concentrated on preexisting fractures.

The shallow deformations lie within the "limits" of the 'excavation damage zone' (EDZ; Amann et al., 2018). The EDZ around the CS-D niche (where our boreholes are located) was stable by the time of the Gallery 18 breakthrough detailed in this work (Corkum & Martin, 2007). We are therefore observing the response of the stable, preexisting EDZ as it merges with the new, unstable EDZ surrounding the approaching gallery excavation. The strains shown in Figure 3B are the result of these complicated interactions between the new gallery and the preexisting galleries and niches, each with different orientations with respect to the far field stress (Figure 1C) and with respect to the dominant orientation of the Opalinus bedding (striking NE). This leads to a complicated redistribution of the local strains, resulting in extension in some locations (D4, D6) and contraction in others (D3, D5). D3 and D5 are drilled with similar orientations from opposing sides of Niche CO_2 and therefore show a similar shallow strain pattern. D4 and D6 were drilled through portions of the EDZ directly below a gallery and a niche, respectively. Given a vertical σ_1, where the roof and floor of the gallery should converge, it makes sense that D4 and D6 would show extension along the fiber axis. But apart from qualitative observations, a complicated modeling exercise will be required to shed more light on the patterns shown in Figure 3B.

At depths >7 m, strain is localized on several distinct features visible in Figure 3A (indicated by colored arrows). In boreholes D3, D4, and D5, at least one feature is present in a zone that is not the Main Fault, whereas in D6 the Main Fault itself is the only notable feature. In D3, D4, and D5, off-Main Fault deformations are >100 $\mu\epsilon$, comparable to and exceeding the strain measured within the Main Fault zone. Approximately 18% of the off-Main Fault fractures identified in core logs correspond to the features indicated by arrows in Figure 3A.

In all boreholes, strain localizes on the uppermost interface of the fault zone. In D5, ~240 microstrain accumulates on this surface, with lesser magnitudes in the other boreholes. Strain also localizes on the lower interface of the fault zone, with relatively little strain measured within the fault zone itself.

Compared to the other boreholes, strain in D6 (particularly on the upgoing fiber) appears more distributed over the entire fault zone. D6 is vertical and therefore oblique to the Main Fault. The fiber axis in D6 is therefore more closely aligned with the fault

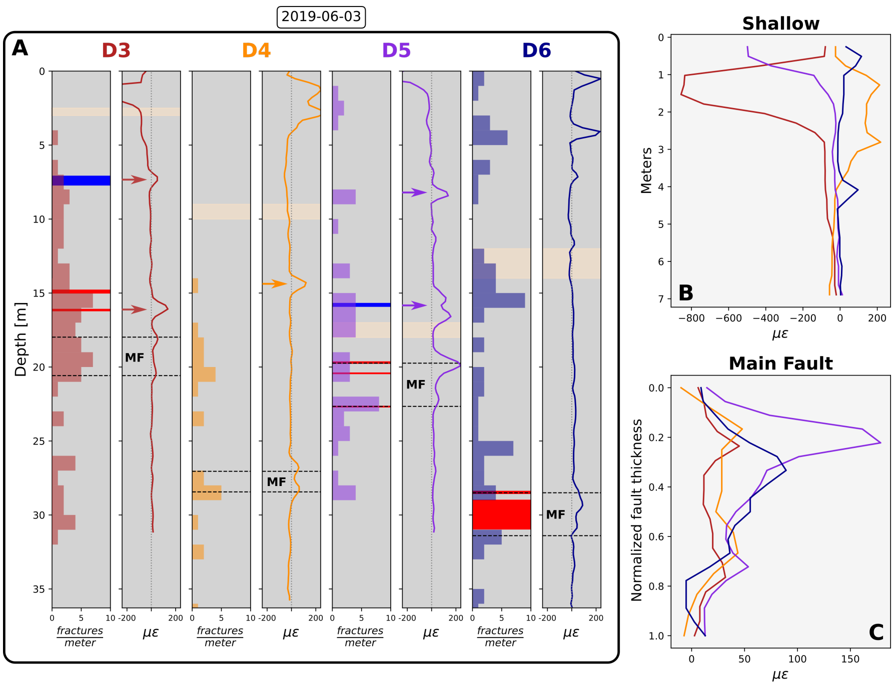

Figure 3. On and off-fault strains - A) Measured strain and fracture density estimated from core. Solid red lines indicated depths of scaly clay identified during core characterization, blue indicates a fracture zone (when not also identified with scaly clay) D4 was drilled with destructive methods so we report fracture density from optical televiewer logs. Resin plugs are in beige, fault top and bottom are indicated by horizontal dotted lines. Arrows show above-fault features recorded on both the up and down-going fibers B) Strains for the upper 7 m of each borehole C) Strains within the fault zone for each borehole. Depths are normalized to the fault zone thickness in each borehole.

interface than in D3, D4, or D5, meaning that it may better capture small amounts of shear distributed within the entire fault zone.

6.2 Comparison of DSS measurements to other instruments

In Figure 4A, we show both the chain potentiometer (red) and DSS measurements (purple) in BCS-D5 on 3 June 2019 following excavation breakthrough. The fracture density as estimated from analysis of drill core is shown as a grey histogram. The potentiometer string has a variable spatial resolution defined by the spacing of the anchor points between individual elements. We plot these data as a series of steps to account for this. The spacing between elements is smallest across the Main Fault interval (0.5 m). Two other elements of roughly 8 m length are placed above the fault. At the depth of the Main Fault interval, the chain potentiometer and fiber optic measurements both clearly show that most of the movement within the fault interval is concentrated at the uppermost interface, where displacements of 282 μm and 210 μm are measured, respectively. A smaller magnitude peak is also observed at the bottom fault interface, respectively of 80 and 67 μm on the potentiometer and DSS. Above the fault, the DSS retains its 1 m spatial resolution, whereas the potentiometer averages displacements over two 8 meter intervals (from 11–19 m and 2–11 m). Two other large deformations are measured by the DSS; one just above the resin plug (16–17 m) and one at 8 m depth. The chain potentiometer, on the other hand, measures no displacement over its shallow intervals due to its lack of spatial resolution.

Figure 4B shows a time series comparison between the DSS and the potentiometer in BCS-D5. We integrated over the three potentiometer elements at 19.75, 20.25, and 20.75 m depths and did the same for the DSS across this depth interval to produce the displacement traces shown. The match between the two instruments is excellent, with a normalized cross correlation coefficient of 0.996 that, when combined with the match shown in Figure 4A, is an indication that the strain magnitudes measured by the DSS system are accurate (if we accept the industry standard potentiometer as a ground-truth). This shows that the DSS can accurately quantify the strain field, thereby complementing results from previous studies where DSS could be used only in a qualitative manner (Krietsch et al., 2018; Valley et al., 2012).

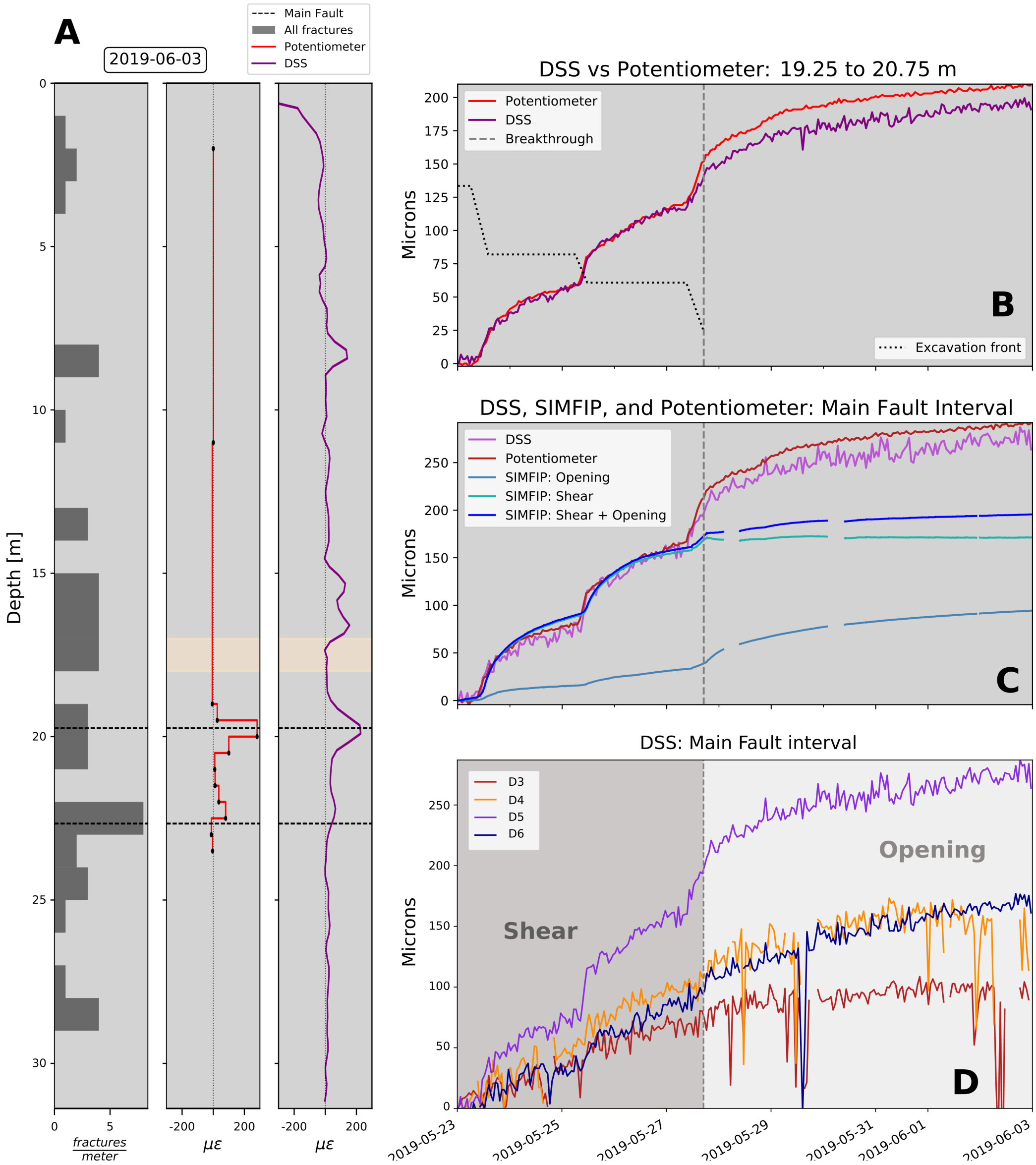

Figure 4. Fault response to gallery excavation - A) Comparison between fracture density, potentiometer extensional strain and DSS strain six days after the breakthrough of Gallery 18 at Niche CO_2. B) Time series comparison between DSS and potentiometer integrated between 19.25 and 20.75 m depth in D5. The dotted line shows the distance of the excavation front to the top of the fault at BCS-D5. The dashed line is the time of the breaktrough C) Potentiometer, DSS, and SIMFIP measurements over the fault zone. SIMFIP total shear is light green and borehole-parallel displacement is gray-blue. The dark blue curve shows the synthetic DSS measurement modeled from SIMFIP data. D) Comparison of DSS displacements integrated across the fault zone in all boreholes.

In figure 4D, we compare the temporal evolution of the DSS data integrated across the Main Fault zone thickness. The Main Fault at D5, being closer to the source of stress perturbation, shows a larger displacement than the other boreholes. From the perspective of the DSS fibers, the change in the mode of fault movement is not noticeable. This is because the fiber measurement is sensitive only to changes along the fiber axis. The fiber system is obviously sensitive to shear in the Main Fault (see D5, in purple, during the shear-mode period in the Figure 4D). But the sense of shear, or the transition to open-mode deformation, is impossible to discern from a single fiber optic sensor.

Figure 5 shows the observed deformations in 3-dimensions. Figure 5A shows results for 25 May 2019, before the breakthrough, while Figure 5B shows observations from 27 May 2019, just after breakthrough. The polygons on the left show the distribution of displacement on a plane parallel to the fault. For each hour, we performed a linear interpolation between the integrated DSS measurements in each borehole and the vector sum of the SIMFIP displacements (all of which are shown in Figure 4C and D). While the spatial extent of the boreholes is fairly limited, there is a clear negative gradient in fault zone displacement from left to right (SW to NE) and top to bottom (shallower to deeper). This is consistent with the orientation of the excavation front, approximately indicated by the red arrow, which is closest to the Main Fault intersection with D5 and therefore induces the largest stress perturbation at that point. The black arrow is the projection of the SIMFIP displacement onto the fault plane for the preceding hour. This displacement represents an oblique reverse sense of shear across the fault zone, pointing in the direction of greatest stress perturbation, in good agreement with the deformation gradient. Following breakthrough, little shear was observed on the Main Fault.

We also plot the DSS data in cross section, superimposed on the trajectories of the boreholes (Figure 5; righthand column). The SIMFIP displacement vector (in the plane of the cross section) is again shown as a black arrow. The Main Fault interfaces, defined by their logged depths, are overlain in dotted gray. We also overlay the approximate orientation of the bedding of the Opalinus clay (measured orientation: N055^o, dipping SE046^o; green dotted lines, Nussbaum et al., 2011). The depths of the bedding planes shown are solely schematic, but we have overlain them in such a way that they might correspond to peaks in strain above the depth of the Main Fault. We suggest that these features correspond to bedding-parallel fractures that were re-activated by the excavation (Amann et al., 2018). The peaks in the strain curves are not present at all boreholes for some of

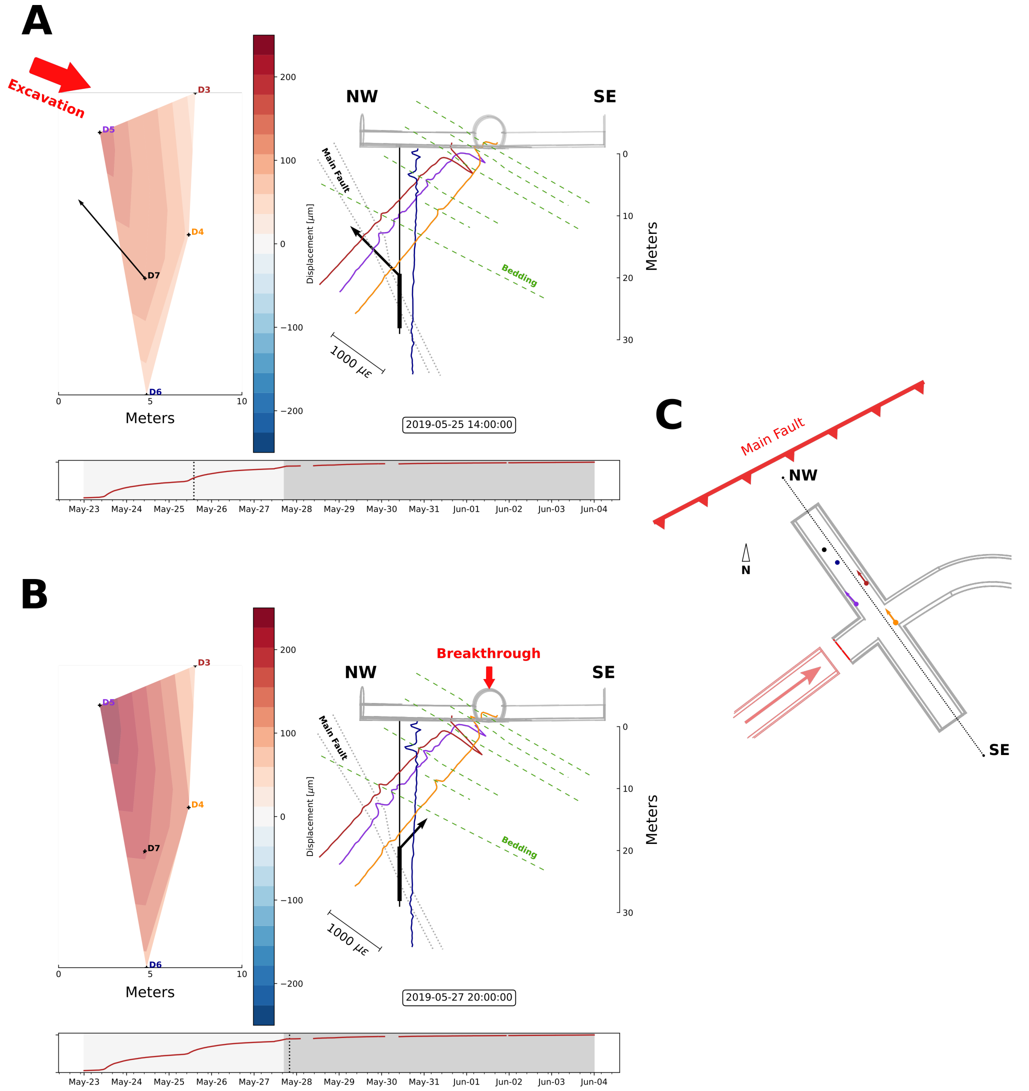

Figure 5. A) Deformation before the excavation breakthrough (26 May) and B) after (1 June; bottom row). The left column shows displacement along the fault plane, linearly interpolated between boreholes. The right column shows a cross-section along Niche CS-D with the strain curves in Figure 3 projected onto the boreholes. Borehole D7 is shown in gray with the SIMFIP indicated by the black box. The direction of SIMFIP displacement (magnitude not to scale) is shown as a black arrow, projected onto the fault plane and the cross-section in the left and right columns, respectively. C) Overview map of Niche CO_2 with the location of the excavated gallery, Main Fault, and boreholes.

these proposed fractures, but we note that strain on the Main Fault (for which orientation and depth are well constrained) is equally varied between boreholes. These bedding parallel fractures are pervasive in the Opalinus clay and represent a later stage of deformation than the Main Fault, possibly even cross cutting it (Nussbaum et al., 2011).

7 Discussion

7.1 DSS sensitivity to shear and slow slip

Although fiber optics are only able to measure changes along the axis of the fibers themselves (i.e. lengthening or shortening), they can potentially capture shear if the deformation field is not perfectly aligned with the fiber's axis. This is typically the case when shear is localized on fractures and faults that intersect the monitoring boreholes at oblique angles. The nature of DSS measurements in shear has been tested in the lab (e.g. Madjdabadi et al., 2016), but only for a fiber anchored between two points, not grouted over tens of meters.

Here, the SIMFIP instrument installed in BCS-D7 offers a unique opportunity to estimate the amount of shear applied to the DSS fiber in BCS-D5. We first make the assumption that the displacement measured across the Main Fault at BCS-D7 can be used as a proxy for displacement at BCS-D5, although the distance between the boreholes is roughly seven meters along the fault interface and the fault interface dips more steeply in D5 than in D7. We rotate the SIMFIP displacement tensor into the borehole coordinates of BCS-D5, such that one component is parallel to the borehole axis and the other two are perpendicular. We then compute the total displacement perpendicular to the borehole (i.e. total shear). We add the borehole-parallel and borehole-normal components of the rotated SIMFIP tensor (vector summation) to give the blue curve that is shown in Figure 4C. To directly compare this synthetic with the actual DSS and potentiometer measurements, we integrate both across the fault interval. The DSS and potentiometer curves in Figure 4C, still in excellent agreement when integrated across the fault, closely match the blue SIMFIP curve for the first two excavation pulses. This corresponds to the period of shear-mode deformation of the Main Fault. This tells us that the distributed DSS and potentiometer measurements are sensitive to more than simply borehole-parallel displacements, instead measuring the correct magnitude of applied shear as well. Interestingly, for the final period of excavation, when the SIMFIP measured mostly normal-mode opening, the potentiometer and DSS measure much larger displacements. We suggest two potential causes of this discrepancy:

1. The fault slips differently at D5 than at D7 and we cannot simply assume the SIMFIP measurements accurately reflect movement even a few meters away. Indeed, the surface of the Main Fault is actually quite complex. For example, the upper fault interface at D5 strikes N244^o and dips 81^{o}NW (possibly overturned) while in D7 it is more consistent with the overall Main Fault trend (strike N037^o, dip 64^{o}SE; Zappone et al., 2020). The opposing dips at the two boreholes may lead to completely different slip mechanisms in response to the gallery excavation, perhaps with shear continuing at D5 where none occurs at D7.
2. The distributed nature of the potentiometer and DSS allow them to measure different phenomena than the SIMFIP, which only senses between two points. The onset of opening mode deformation indicates a significant change in the stress state acting on the fault and may be activating fractures within the fault zone that weren't active during the shear stage, or changing their mode of deformation.

7.2 Architecture and behavior of a clay-hosted fault zone

The DSS measurements indicate that the two interfaces of the Main Fault zone accommodate most of the fault slip related to the gallery excavation, with no single, central slip surface. This is particularly evident in the inclined boreholes D3, D4, and D5 (Figure 3c). In all cases, strain decays quickly away from the fault interfaces. Slip on the upper Main Fault interface, being closer to the excavation, probably relieved some of the stress that otherwise would have been transmitted to the lower interface, thereby producing an apparent gradient, with higher strain concentrated on the upper interface. In addition, this stress shadow effect may explain the lack of strain measured below the fault, even in the presence of identified fractures deeper in the boreholes. This pattern of slip on the bounding interfaces, as opposed to on a central slip surface, may relate to the Main Fault architecture.

Indeed, as schematized in Figure 6, fault zones are commonly conceptualized as a fault core, where the majority of the slip concentrates, and a surrounding damage zone that accommodates progressively less slip with distance from the core (Caine et al., 1996; Shipton & Cowie, 2003). The Main Fault of the MTRL, however, has an altogether different architecture, with a thick, heterogeneous layer bounded by two weak interfaces (Fig. 6). These interfaces comprise a layer of fault gouge and scaly clay (up to 1 cm thick; Wenning et al., 2020) that abut undisturbed Opalinus clay host rock (Jaeggi et al., 2017; Nussbaum et al., 2011; Amann et al., 2018). Between the two bounding planes, the fault is a complex mixture of scaly clay fabric and secondary fractures (also filled with scaly clay). Outside the bounding planes is intact rock with no damage zone transition. In addition, previous experiments at the MTRL indicate that the fault zone has a Young's modulus 2–5 times less than the host rock (Jeanne et al., 2017). Observed DSS strains may result from the high compliance of the fault zone relative to the host rock. During the gallery excavation, for example, stress unloading would lead to 'bulging' of the fault zone and slip at the interfaces. These lines of evidence suggest that the Main Fault should be treated as a thick, soft layer bounded by weak boundaries and no surrounding damage zone.

A number of secondary fracture sets exist within the Main Fault (Wenning et al., 2020) that might produce complex deviations from deviations from the observed 'two-peaked' pattern, for example explaining the strain measured in the fault zone at D6 (Figure 3C). In addition, the interaction of the bedding-parallel fracture set (cross sections; Figure 5) with the Main Fault is not well understood. Given that the bedding-parallel fractures represent a later stage of deformation, they may cross cut the Main Fault itself (Nussbaum et al., 2011) and accommodate some deformation affecting the Main Fault interval.

7.3 Stress controls on fracture activation in the Opalinus clay

In many cases, the strain that accumulated on secondary (i.e. non-Main Fault) fractures exceeded that of the Main Fault interfaces. For example, the 16-m anomaly in D3 displays nearly twice the displacement of the top or bottom interfaces of the Main Fault. In addition, the anomalies in D4 and D5 display similar deformation magnitudes to the Main Fault zone. Although a number of these secondary structures were activated, the vast majority of those identified in logs were not. For a given fracture, activation is controlled by its orientation in the local stress state and its intrinsic properties (e.g. cohesion, coefficient of friction; Handin, 1969; Freed, 2005), but identifying which will activate for given stress perturbation is difficult.

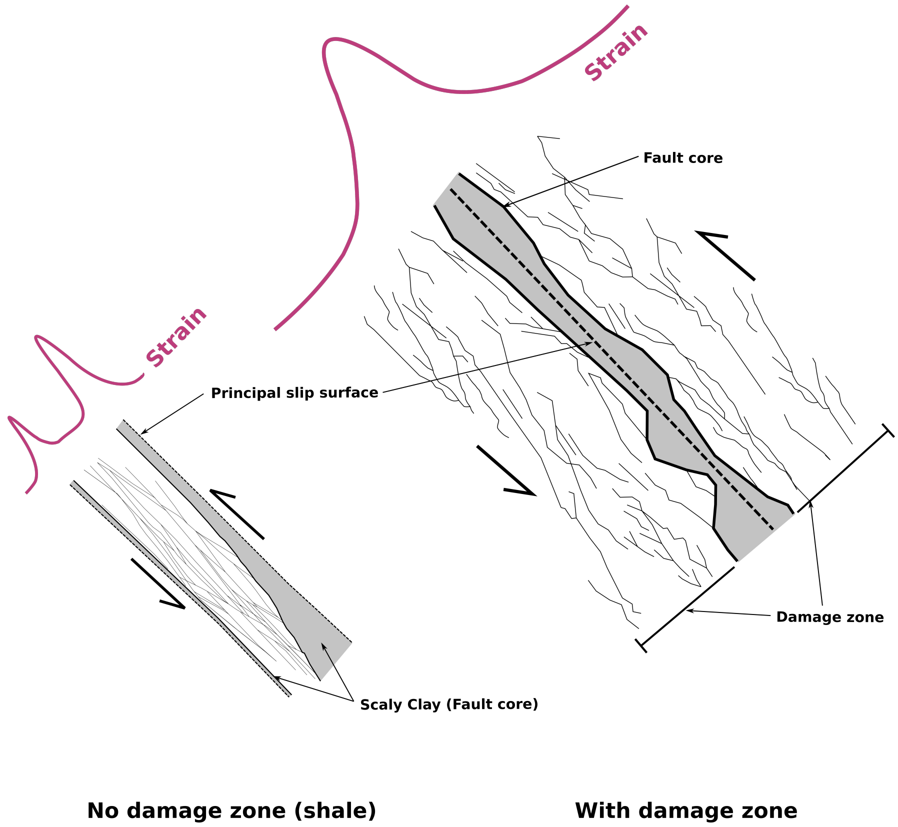

Figure 6. Schematic representations of the Main Fault (left; adapted from Jaeggi et al., 2017)) and the canonical fault zone model (right; adapted from Shipton & Cowie, 2003) showing the relationship between fault core/gouge, principal slip surfaces, and the 'fault damage' zone. Theoretical DSS measurements are shown in purple for slip on either type of fault.

Geological interpretation of the core classifies the deepest non-fault feature in BCS-D3 (16 m depth) as an interval of scaly clay layers. Optical televiewer (OTV) images for D3 were too poor for accurate picking. The single shallow feature in D4, as identified in OTV logs, corresponds to a single fracture striking N052^o, dipping SE69^o. The 15–16-m depth interval in BCS-D5 is classified as a distinct fault zone, four meters above the Main Fault (strike N014–060^o, dip 20–70^{o}SE). The 8-meter anomaly in D5 corresponds to a series of features classified as either 'bedding' or 'fracture planes' in the core (strikes N053–082^o, dips 54–74^{o}SE).

To investigate what distinguished the active fractures from the non-active ones, we separate all OTV-picked fractures into three groups: those inside the fault zone, active fractures outside the fault zone, and inactive fractures outside the fault zone. Figure 7 shows each plane identified in the BCS-D4, D5, and D6 optical televiewer logs colored by slip tendency (increasing from blue to red) when subjected to the stress field determined by Guglielmi et al. (2020) for the MTRL.

As detailed by Wenning et al. (2020), the Main Fault zone includes a variety of fracture sets of varying orientations, including fault-zone parallel fractures and WNW-dipping fractures, which are the most prone to slip of any of the identified features (red features, Figure 7A). As we mentioned above, however, slip localized on the upper and lower fault zone interfaces, which are further from failure in the in-situ stress conditions (dashed black lines and adjacent green lines, Figure 7).

The off-fault fractures predominantly strike NE, with dips ranging from $\sim$10–70^o (Figure 7B-C). In a static stress state, the features that displayed a DSS signal are no more likely to slip than those which showed no deformation, making it difficult to discern in advance, solely from OTV logs, which features would be most likely to slip. These sets of features also span the orientation of both bedding and the Main Fault zone, meaning we cannot confidently state whether one or the other is hosting the deformation that is being measured. This is partially an effect of the DSS spatial resolution, which prevents us from assigning strain to single features located within the 1-m gauge length of a DSS peak and may obscure subtle variations between slipping and non-slipping features.

Because the induced stress perturbation decreases with distance from the excavation, we color each feature in the lower row of Figure 7 by its distance from the breakthrough point. The features in column B, associated with strain signals outside the fault zone, are closer to the excavation front (on average, shown by their lighter color) than either the Main Fault itself, or the features displaying no strain. This suggests that, for features outside the weak fault zone, the distance to the stress perturbation has a weak control on whether they activate.

The failure criterion used in Figure 7 assumes cohesionless fractures with a coefficient of friction of 0.45, taken as a representative value from Opalinus core testing performed by Orellana et al. (2018). Nearly all of the activated structures fall well below the failure criterion, suggesting that either the stress perturbation from the excavation was on the order of multiple MPa, that the activated fractures are actually intrinsically weaker than our simple analysis suggests, or (likely) both. Careful characterization of the core indicates that most of the activated structures are associated with either 1) a lens of scaly clay, consisting of shear-realigned grains (Jaeggi et al., 2017; Laurich et al., 2018) or 2) highly fractured zones where core was either lost or fragmented (red and blue solid lines in Figure 3A, respectively). The production of scaly clay is a product of shear, and produces a zone of weakness onto which further slip will tend to accumulate (Laurich et al., 2018). It is therefore possible that the fractured zones also contained small amounts of scaly clay that were not adequately recovered during coring and therefore were not classified as such. In any case, the correlation between DSS anomoalies and the depth of known lenses of scaly clay (Figure 3A) suggests the presence of scaly clay is the main controlling factor on fracture weakness and therefore on which features most likely to activate under remote loading. At the MTRL, scaly clay has developed on both bedding parallel fractures and the Main Fault-parallel structures, despite their somewhat distinct orientations. This makes both sets of features susceptible to reactivation, and candidates for fluid flow within the Opalinus clay.

8 Conclusions

We presented measurements from seven boreholes intersecting a fault zone in clay rock at the Mont Terri Rock Laboratory in Switzerland. Our dataset encompasses a period of new gallery excavation that remotely triggered slip within the fault and fractures affecting the thick shale series. One chain potentiometer and one high-resolution 3D displacement sensor, installed alongside the fibers, allowed us to tune the magnitudes of the strain measurements made via DSS.

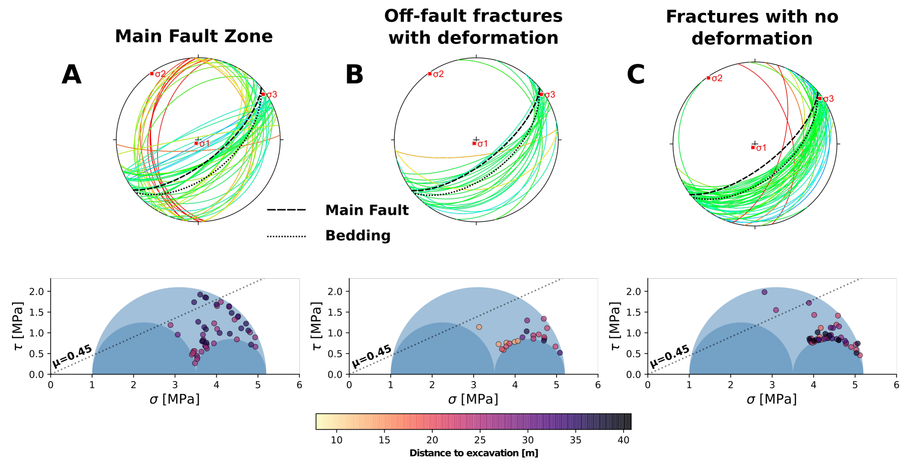

Figure 7. Fractures identified in optical televiewer logs in BCS-D4, D5, and D6 - A) Within the Main Fault zone B) outside of the Main Fault but displaying deformation on DSS C) All other fractures. The upper plots are lower hemisphere projections of poles and planes, colored by slip tendency in the local stress regime estimated by Guglielmi et al. (2020) (blue=low, red=high tendency). Dotted line shows the orientation of bedding at the MTRL, the dashed line shows the approximate orientation of the Main Fault. The lower row plots show the state of stress on each fracture relative to a Mohr Coulomb failure envelope for cohesionless fractures. Following Orellana et al. (2018), a peak coefficient of friction of μ=0.45 is used. The color of each dot corresponds to the distance from the feature to the excavation front (light=closer, dark=further).

During the excavation, located about 30 m away from our instrumented boreholes, strains ranging from 50–240 $\mu\epsilon$ were measured mainly at the top and bottom of the fault zone at each of our boreholes, well above the maximum 3σ noise level of $\sim$20 $\mu\epsilon$. We showed that the DSS measurement has a significant sensitivity to shear strain in a grouted borehole and thus can be used to estimate fault slip. The complex mechanical response of the gallery excavation damage zone was also captured on the DSS. Indeed, our tuned measurements also provide insight into the reactivation behavior of a clay-hosted fault.

The DSS measurements show that slip localized on several discrete fractures identified in core and logs. Within the Main Fault, slip concentrated on the upper and lower fault zone interfaces, with relatively little deformation occurring inside the fault zone. Core samples revealed zones of fault gouge on these interfaces, indicating past episodes of slip and present-day mechanical weakness. The DSS measurements support a fault model consisting of a single, thick fault zone with no surrounding damage zone. Slip occurs at both interfaces between the fault zone and the undisturbed host rock, possibly due to bulk deformation of the relatively compliant fault zone geology. This is in contrast to the canonical fault model for harder rocks where most slip occurs on a central fault core surrounded by a damage zone.

Away from the fault, deformation concentrated at depths associated with lenses of scaly clay or highly-fractured intervals (as indicated in core samples), likely on bedding-parallel fractures. Most fractures identified in OTV logs were not reactivated, despite nearly all having a similar orientation with respect to stress. Therefore, we conclude that fracture reactivation during the excavation was controlled by the intrinsic properties of the fractures, likely the presence or absence of scaly clay and fault gouge resulting in a low-cohesion, low-friction surface.

Previous grouted DSS measurements have only proven to be of qualitative use. In contrast to these previous studies, we show how a grouted network of fiber optic cables can complement other monitoring systems to quantify the subsurface strain field. While additional case studies like ours are necessary to expand the existing understanding of these fiber optic measurements, they should prove useful in monitoring the impacts of slow slip on fault-hosted leakage and induced seismicity in shales.

Acknowledgments

The authors are deeply grateful to the partners of the Mont Terri Project that contributed to the funding of the CS-D and FS-B experiments: the Swiss Federal Office of Topography (Swisstopo), the Swiss Federal Nuclear Safety Inspectorate (ENSI), the Japanese Atomic Energy Agency (JAEA), the Institute of Radioprotection and of Nuclear Safety (IRSN, France), TOTAL SE, CHEVRON, the Federal Institute for Geosciences and Natural Resources (BGR, Hannover), the Swiss Federal Institute of Technology (ETH Zurich), and the U.S. Department of Energy. The Mont Terri Project is an international research project for the hydrogeological, geochemical, and geotechnical characterizations of a clay formation (Opalinus clay). Funding for Berkeley Lab's analysis of the FS-B data described in this study was provided by the Assistant Secretary for Fossil Energy as part of the Core Carbon Storage and Monitoring Research (CCSMR) and National Risk Assessment Partnership (NRAP) programs of the U.S. Department of Energy under contract FP00007630. Experimental data are available in the supporting information. The CS-D experiment is part of the ACT ELEGANCY, Project No 271498. This project is supported by the Pilot and Demonstration Programme of the Swiss Federal Office of Energy (SFOE).

The stereonet and Mohr-Coulomb plots for Figure 7 were generated using Rick Allmendinger's software packages Stereonet and MohrPlotter, found here: https://www.rickallmendinger.net (Allmendinger et al., 2011).

Access to the datasets presented in this paper will be made available via a public server at ETH Zurich prior to acceptance of this manuscript.

References

Allmendinger, R. W., Cardozo, N., & Fisher, D. M. (2011). *Structural Geology Algorithms*. Cambridge University Press. Retrieved from `https://doi.org/10.1017%2Fcbo9780511920202` doi: 10.1017/cbo9780511920202

Amann, F., Wild, K. M., Loew, S., Yong, S., Thoeny, R., & Frank, E. (2018). Geomechanical behaviour of opalinus clay at multiple scales: results from mont terri rock laboratory (switzerland). In *Mont terri rock laboratory, 20 years* (pp. 153–173). Springer.

Birkholzer, J. (2018). Can Induced Seismicity Cause Fault Leakage and How Does it Evolve with Time? In *14th greenhouse gas control technologies conference mel-*

bourne (pp. 21–26).

Bossart, P., Bernier, F., Birkholzer, J., Bruggeman, C., Connolly, P., Dewonck, S., … Wieczorek, K. (2017, dec). Mont Terri rock laboratory 20 years of research: introduction, site characteristics and overview of experiments. In *Mont terri rock laboratory, 20 years* (pp. 3–22). Springer International Publishing. Retrieved from https://doi.org/10.1007%2F978-3-319-70458-6_1 doi: 10.1007/978-3-319-70458-6_1

Bourg, I. C. (2015). Sealing shales versus brittle shales: a sharp threshold in the material properties and energy technology uses of fine-grained sedimentary rocks. *Environmental Science & Technology Letters*, *2*(10), 255–259.

Caine, J. S., Evans, J. P., & Forster, C. B. (1996). Fault zone architecture and permeability structure. *Geology*, *24*(11), 1025–1028.

Corkum, A., & Martin, C. (2007, sep). Modelling a mine-by test at the Mont Terri rock laboratory Switzerland. *International Journal of Rock Mechanics and Mining Sciences*, *44*(6), 846–859. Retrieved from https://doi.org/10.1016%2Fj.ijrmms.2006.12.003 doi: 10.1016/j.ijrmms.2006.12.003

Delepine-Lesoille, S., Phéron, X., Bertrand, J., Pilorget, G., Hermand, G., Farhoud, R., … Lanticq, V. (2012). Industrial Qualification Process for Optical Fibers Distributed Strain and Temperature Sensing in Nuclear Waste Repositories. *Journal of Sensors*, *2012*, 1–9. Retrieved from https://doi.org/10.1155%2F2012%2F369375 doi: 10.1155/2012/369375

Freed, A. M. (2005, may). EARTHQUAKE TRIGGERING BY STATIC DYNAMIC AND POSTSEISMIC STRESS TRANSFER. *Annual Review of Earth and Planetary Sciences*, *33*(1), 335–367. Retrieved from https://doi.org/10.1146%2Fannurev.earth.33.092203.122505 doi: 10.1146/annurev.earth.33.092203.122505

Guglielmi, Y., Birkholzer, J., Rutqvist, J., Jeanne, P., & Nussbaum, C. (2017, jul). Can Fault Leakage Occur Before or Without Reactivation? Results from an in Situ Fault Reactivation Experiment at Mont Terri. *Energy Procedia*, *114*, 3167–3174. Retrieved from https://doi.org/10.1016%2Fj.egypro.2017.03.1445 doi: 10.1016/j.egypro.2017.03.1445

Guglielmi, Y., Cappa, F., Lançon, H., Janowczyk, J. B., Rutqvist, J., Tsang, C. F., & Wang, J. S. Y. (2013). ISRM Suggested Method for Step-Rate

Injection Method for Fracture In-Situ Properties (SIMFIP): Using a 3-Components Borehole Deformation Sensor. In *The ISRM suggested methods for rock characterization testing and monitoring: 2007-2014* (pp. 179–186). Springer International Publishing. Retrieved from `https://doi.org/10.1007%2F978-3-319-07713-0_14` doi: 10.1007/978-3-319-07713-0_14

Guglielmi, Y., Nussbaum, C., Jeanne, P., Rutqvist, J., Cappa, F., & Birkholzer, J. (2020, feb). Complexity of Fault Rupture and Fluid Leakage in Shale: Insights From a Controlled Fault Activation Experiment. *Journal of Geophysical Research: Solid Earth*, *125*(2). Retrieved from `https://doi.org/10.1029%2F2019jb017781` doi: 10.1029/2019jb017781

Guglielmi, Y., Nussbaum, C., Robertson, M., Ajo-Franklin, J., Zappone, A., Kloppenburg, A., & Birkholzer, J. (2018). *FS-B Experiment: Imaging the long-term loss of faulted host rock integrity - Test plan, Mont Terri Technical Note* (Tech. Rep. No. TN2018-20).

Gutierrez, M., Øino, L., & Nygaard, R. (2000). Stress-dependent permeability of a de-mineralised fracture in shale. *Marine and Petroleum Geology*, *17*(8), 895–907.

Handin, J. (1969, oct). On the Coulomb-Mohr failure criterion. *Journal of Geophysical Research*, *74*(22), 5343–5348. Retrieved from `https://doi.org/10.1029%2Fjb074i022p05343` doi: 10.1029/jb074i022p05343

Hartog, A. H. (2017). *An Introduction to Distributed Optical Fibre Sensors.* CRC Press. Retrieved from `https://doi.org/10.1201%2F9781315119014` doi: 10.1201/9781315119014

Horiguchi, T., & Tateda, M. (1989). BOTDA-nondestructive measurement of single-mode optical fiber attenuation characteristics using Brillouin interaction: theory. *Journal of Lightwave Technology*, *7*(8), 1170–1176. Retrieved from `https://doi.org/10.1109%2F50.32378` doi: 10.1109/50.32378

Hostettler, B., Reisdorf, A. G., Jaeggi, D., Deplazes, G., Bläsi, H., Morard, A., … Menkveld-Gfeller, U. (2017, feb). Litho- and biostratigraphy of the Opalinus Clay and bounding formations in the Mont Terri rock laboratory (Switzerland). *Swiss Journal of Geosciences*, *110*(1), 23–37. Retrieved from `https://doi.org/10.1007%2Fs00015-016-0250-3` doi: 10.1007/s00015-016-0250-3

Iten, M., Puzrin, A. M., & Schmid, A. (2008, mar). Landslide monitoring using a road-embedded optical fiber sensor. In W. Ecke, K. J. Peters, & N. G. Meyendorf (Eds.), *Smart sensor phenomena technology, networks, and systems 2008.* SPIE. Retrieved from `https://doi.org/10.1117%2F12.774515` doi: 10.1117/12.774515

Jaeggi, D., Laurich, B., Nussbaum, C., Schuster, K., & Connolly, P. (2017, jan). Tectonic structure of the "Main Fault" in the Opalinus Clay Mont Terri rock laboratory (Switzerland). *Swiss Journal of Geosciences*, *110*(1), 67–84. Retrieved from `https://doi.org/10.1007%2Fs00015-016-0243-2` doi: 10.1007/s00015-016-0243-2

Jeanne, P., Guglielmi, Y., Rutqvist, J., Nussbaum, C., & Birkholzer, J. (2017). Field characterization of elastic properties across a fault zone reactivated by fluid injection. *Journal of Geophysical Research: Solid Earth*, *122*(8), 6583–6598.

jun Wang, B., Li, K., Shi, B., & qing Wei, G. (2008, sep). Test on application of distributed fiber optic sensing technique into soil slope monitoring. *Landslides*, *6*(1), 61–68. Retrieved from `https://doi.org/10.1007%2Fs10346-008-0139-y` doi: 10.1007/s10346-008-0139-y

Krietsch, H., Gischig, V., Jalali, M., Doetsch, J., Valley, B., Amann, F., et al. (2018). A comparison of FBG-and Brillouin-strain sensing in the framework of a decameter-scale hydraulic stimulation experiment. In *52nd us rock mechanics/geomechanics symposium.*

Laurich, B., Urai, J. L., Vollmer, C., & Nussbaum, C. (2018). Deformation mechanisms and evolution of the microstructure of gouge in the main fault in opalinus clay in the mont terri rock laboratory (ch). *Solid Earth*, *9*(1), 1–24.

Madjdabadi, B., Valley, B., Dusseault, M., & Kaiser, P. (2014). Numerical study of grout–rock mass interaction effect on distributed optical fibre sensor measurements. In *Proceedings of the seventh international conference on deep and high stress mining.* Australian Centre for Geomechanics Perth. Retrieved from `https://doi.org/10.36487%2Facg_rep%2F1410_31_madjdabadi` doi: 10.36487/acg_rep/1410_31_madjdabadi

Madjdabadi, B., Valley, B., Dusseault, M. B., & Kaiser, P. K. (2016, jan). Experimental evaluation of a distributed Brillouin sensing system for measuring extensional and shear deformation in rock. *Measurement*, *77*, 54–66. Retrieved from https://doi.org/10.1016%2Fj.measurement.2015.08.040 doi: 10.1016/j.measurement.2015.08.040

Naruse, H. (1999, sep). River levee strain measurement using fiber optic distributed strain sensor. In *13th international conference on optical fiber sensors.* SPIE. Retrieved from https://doi.org/10.1117%2F12.2302056 doi: 10.1117/12.2302056

Naruse, H., Komatsu, K., Fujihashi, K., & Okutsu, M. (2005, may). Telecommunications tunnel monitoring system based on distributed optical fiber strain measurement. In *17th international conference on optical fibre sensors.* SPIE. Retrieved from https://doi.org/10.1117%2F12.623645 doi: 10.1117/12.623645

Nussbaum, C., Bossart, P., Amann, F., & Aubourg, C. (2011, sep). Analysis of tectonic structures and excavation induced fractures in the Opalinus Clay Mont Terri underground rock laboratory (Switzerland). *Swiss Journal of Geosciences*, *104*(2), 187–210. Retrieved from https://doi.org/10.1007%2Fs00015-011-0070-4 doi: 10.1007/s00015-011-0070-4

Orellana, L., Scuderi, M., Collettini, C., & Violay, M. (2018). Frictional properties of opalinus clay: Implications for nuclear waste storage. *Journal of Geophysical Research: Solid Earth*, *123*(1), 157–175.

Rinaldi, A. P., Guglielmi, Y., Zappone, A., Soom, F., Robertson, M., Cook, P., ... Nussbaum, C. (2020, mar). Coupled processes in clay during tunnel excavation. Copernicus GmbH. Retrieved from https://doi.org/10.5194%2Fegusphere-egu2020-18041 doi: 10.5194/egusphere-egu2020-18041

Shipton, Z. K., & Cowie, P. A. (2003). A conceptual model for the origin of fault damage zone structures in high-porosity sandstone. *Journal of Structural Geology*, *25*(3), 333–344.

Sun, Y., Xue, Z., Hashimoto, T., Lei, X., & Zhang, Y. (2020, jan). Distributed Fiber Optic Sensing System for Well-Based Monitoring Water Injection Tests—A Geomechanical Responses Perspective. *Water Resources Research*, *56*(1). Retrieved from https://doi.org/10.1029%2F2019wr024794 doi: 10.1029/2019wr024794

Tateda, M., Horiguchi, T., Kurashima, T., & Ishihara, K. (1990). First measurement of strain distribution along field-installed optical fibers using Brillouin spectroscopy. In *Optical fiber communication.* OSA. Retrieved from `https://doi.org/10.1364%2Fofc.1990.pd15` doi: 10.1364/ofc.1990.pd15

Valley, B., Madjdabadi, B. M., Kaiser, P. K., Dusseault, M. B., et al. (2012). Monitoring mining-induced rock mass deformation using distributed strain monitoring based on fiber optics. In *Isrm international symposium-eurock 2012.*

Wenning, Q. C., Madonna, C., Zappone, A., Grab, M., Rinaldi, A. P., Plötze, M., ... Wiemer, S. (2020). Shale fault zone structure and stress dependent anisotropic permeability and seismic velocity properties (opalinus clay, switzerland). *Journal of Structural Geology*, 104273.

Zappone, A., Rinaldi, A. P., Grab, M., Wenning, Q., Roques, C., Madonna, C., ... others (2020). Fault sealing and caprock integrity for co 2 storage: an in-situ injection experiment. *Solid Earth Discussions*, 1–51.

Zhang, C.-C., Shi, B., Gu, K., Liu, S.-P., Wu, J.-H., Zhang, S., ... Wei, G.-Q. (2018, nov). Vertically Distributed Sensing of Deformation Using Fiber Optic Sensing. *Geophysical Research Letters*, *45*(21), 11,732–11,741. Retrieved from `https://doi.org/10.1029%2F2018gl080428` doi: 10.1029/2018gl080428

Zhang, Z., Fang, Z., Stefani, J., DiSiena, J., Bevc, D., Ning, I. L. C., ... Tan, Y. (2020, aug). Modeling of Fiber Optic Strain Responses to Hydraulic Fracturing. *GEOPHYSICS*, 1–22. Retrieved from `https://doi.org/10.1190%2Fgeo2020-0083.1` doi: 10.1190/geo2020-0083.1

Zhou, Z., He, J., Huang, M., He, J., Ou, J., & Chen, G. (2010, mar). Casing pipe damage detection with optical fiber sensors: a case study in oil well constructions. In P. J. Shull, A. A. Diaz, & H. F. Wu (Eds.), *Nondestructive characterization for composite materials aerospace engineering, civil infrastructure, and homeland security 2010.* SPIE. Retrieved from `https://doi.org/10.1117%2F12.848727` doi: 10.1117/12.848727

Zoback, M. D., Kohli, A., Das, I., Mcclure, M. W., et al. (2012). The importance of slow slip on faults during hydraulic fracturing stimulation of shale gas reservoirs. In *Spe americas unconventional resources conference.*

Supplements

Realignment

The next processing step arises in response to potential misalignment of the channels along the fiber. For the majority of our dataset, the spatial sampling is 0.255 meters. This leads to an ambiguity in exactly where the strain is being sensed, which could be ± 0.255 m from the measurement point. We adopt the approach of Madjdabadi et al. (2016) who address this issue through a process of 'realignment'. The measurement $\Delta\nu_i = \nu_{i,j} - \nu_{i,1}$ at channel i and time j is compared to the two adjacent possible changes in absolute Brillouin frequency shift: $\Delta\nu_{i-1} = \nu_{i-1,j} - \nu_{i,1}$ and $\Delta\nu_{i+1} = \nu_{i+1,j} - \nu_{i,1}$. The lowest of these three values is accepted as the final, realigned measurement $\Delta\nu_i$. By applying this algorithm to each time sample, the affect of their observed misalignments was ameliorated.

Gain shifts

Finally, we cleaned a number of artifacts in the dataset resulting from bulk shifts in the intensity of the backscattered light (i.e. gain; Figure S1). These bulk shifts in gain often correlate with bulk shifts in the absolute frequency measured at the interrogator box. In theory, these two values should not be related, but we suspect that there may be a relation between the bulk shifts and the fitting of the Brillouin gain spectrum for each measurement point. Estimation of the peak Brillouin gain, and therefore the Brillouin frequency shift on which the strain measurement relies, is done via a parabolic fitting of the gain spectrum. If the gain is low, and the shape of the spectrum relatively flat and broad, the fitting procedure may be less precise, resulting in the apparent frequency shifts seen in Figure S1, where no real change in strain has occurred. The cause of these shifts is difficult to assess, but they likely happen when portions of the cables that lie in cable trays along the gallery walls are jostled. In particular, we suspect that connectors (not splices) between different cables, when disturbed, can influence the intensity of light returning to the interrogator box, thus producing changes in gain.

To address this, we apply a simple algorithm wherein we identify the bulk gain shifts as any measurement point where the gain changed by 0.014% or greater relative to the previous measurement. At each of these points, we then remove the corresponding strain change from all of the subsequent measurements at that channel.

Period	Spatial resolution [m]	Spatial sampling [m]	Temporal sampling [min]	Averaging	Frequency start [GHz]	Frequency stop [GHz]	Frequency step [MHz]
Gallery excavation	1.0	0.26	60	3000	10.5	11.1	0.5

Table 1. DITEST configuration parameters during the various phases of measurement detailed below. Note that that spatial resolution was changed during the pulse-step test due to high noise levels.

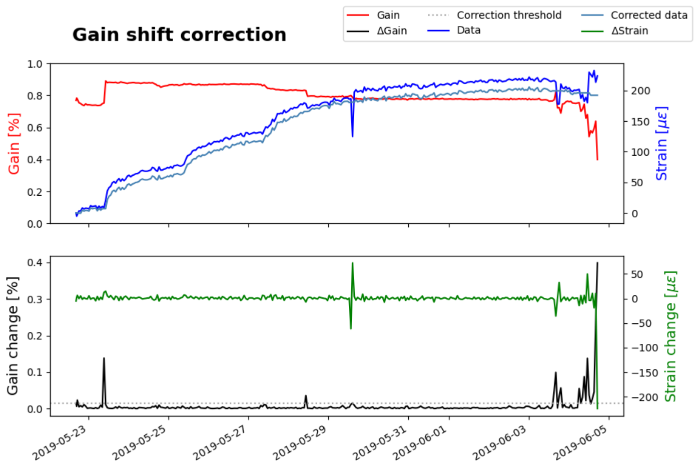

Figure 1. Example channel from BCS-D5 showing A) Gain in red and relative strain in blue prior to the correction for bulk shifts. Light blue shows the corrected data with no shifts at the time of bulk jumps in the gain. B) Shows the differentials of the relative strain in green and gain in black. When gain change exceeded the dotted line (0.014%), we subtracted the change in strain (green) from all subsequent strain measurements (blue).

Core evidence for DSS anomalies

Figure 2 shows core scanner images from the three off-fault intervals in BCS-D3 and D5 that displayed DSS anomalies. The exact intervals are indicated in red boxes.

References

Madjdabadi, B., Valley, B., Dusseault, M. B., & Kaiser, P. K. (2016, jan). Experimental evaluation of a distributed Brillouin sensing system for measuring extensional and shear deformation in rock. *Measurement*, *77*, 54–66. Retrieved from `https://doi.org/10.1016%2Fj.measurement.2015.08.040` doi: 10.1016/j.measurement.2015.08.040

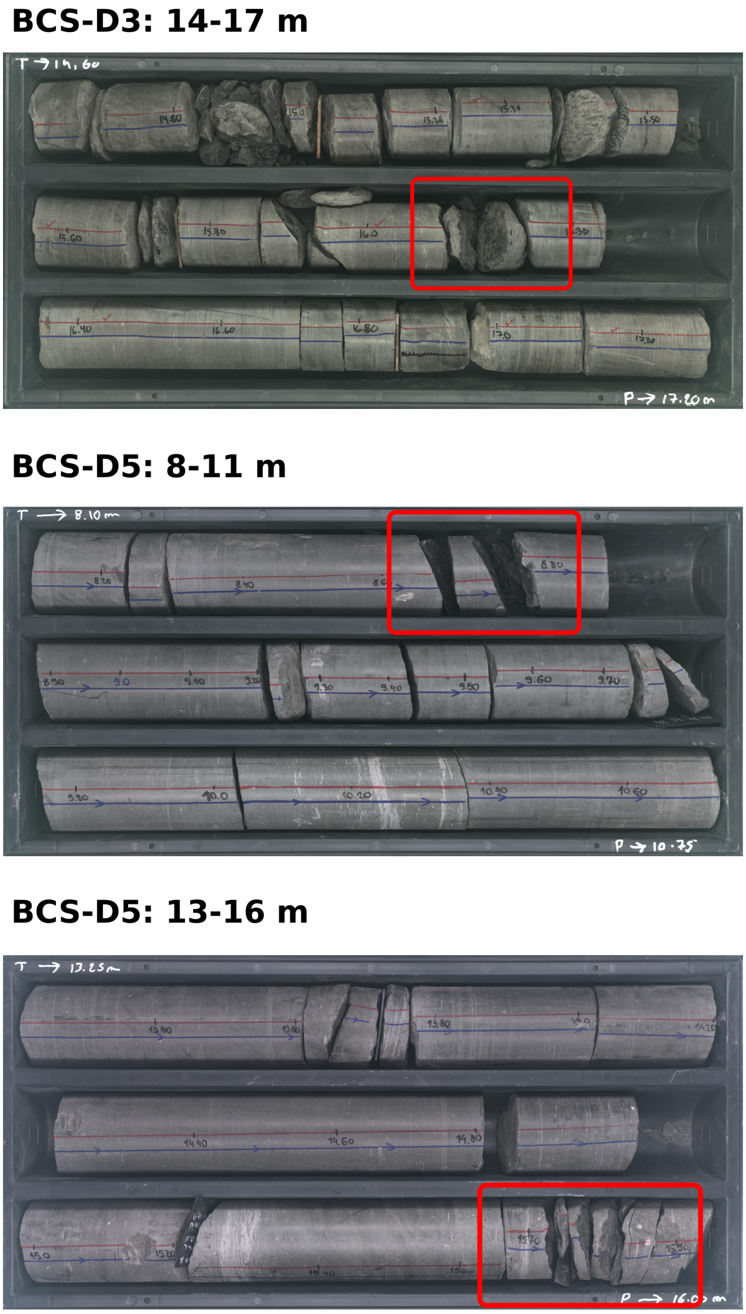

Figure 2. Core scans of the off-fault intervals that displayed measurable strains on the DSS. No core was taken from BCS-D4 and no off-fault anomalies were observed in BCS-D6.